

Research paper

Defects and fault modes of field-aged photovoltaic modules in the Nordics

Oscar Kwame Segbefia^{*}, Naureen Akhtar, Tor Oskar Sætre

Department of Engineering Sciences, University of Agder, 4879 Grimstad, Norway

ARTICLE INFO

Article history:

Received 25 August 2022

Received in revised form 29 November 2022

Accepted 31 January 2023

Available online 13 February 2023

Keywords:

Moisture induced degradation

Microcrack

Silver acetate

Parasitic resistance

Temperature sensitivity

ABSTRACT

PV module durability and reliability influences its efficiency and return on investment. Hence, collection of ample and credible PV module reliability data in each climatic zone becomes increasingly essential. In this work, defects and fault modes of field-aged multicrystalline silicon PV modules installed outdoors in Grimstad from 2000 to 2011 are investigated. The investigations were done using visual inspection, current–voltage characterization, temperature coefficient profiling, ultraviolet fluorescence, electroluminescence, infrared thermal imaging, and SEM-EDS analysis. Most PV modules show signs of microcracks, moisture ingress, corrosion, potential induced degradation, optical degradation, and irregular temperature sensitivities. Oxidized silver, tin, and lead were observed in the SEM-EDS results, which confirmed the remnants of moisture ingress. On average, the modules show power output of ~78% and their efficiency dropped from 13% to ~10%. The average temperature coefficient of efficiency of the module was found to be ca. $-0.5\%/^{\circ}\text{C}$, corresponding to an average degradation rate of 1.09%/year over the 20 years period. However, the annual degradation rates when the modules were in the field and indoors were ~0.98% and ~1.33%, respectively. It is believed that limited evaporation of activated volatile carboxylic products under indoor conditions led to the formation and accumulation of carboxylic acids, hence higher rate of degradation. Moisture induced degradation (MID) mechanisms was the root cause for the overall degradation in the PV modules' power output, especially over the later years.

© 2023 The Author(s). Published by Elsevier Ltd. This is an open access article under the CC BY license (<http://creativecommons.org/licenses/by/4.0/>).

Abbreviations: Ag, silver; Al, aluminum; AM, air mass; ARC, antireflection coating; $C_{(x)}$, optical and material properties of the PV module; C, carbon; CMI, climate moisture index; CNC, Computer Numerical Control software; CO, carbon monoxide; CO_2 , carbon dioxide; DH, damp heat; DSLR, digital single-lens reflex; E, east; EDS, energy dispersive X-ray spectroscopy; EL, electroluminescence spectroscopy; EVA, ethylene vinyl acetate; FEG, Field Emission Gun; FF, fill factor; FTIR, fourier transform infra-red; G_T , in-plane irradiance; H_2O , water; HF, humidity freeze; IEA, International Energy Agency; IEC, International Electrotechnical Commission; I_{mpp} , current at maximum power point; IR, infrared; I_{sc} , short circuit current; I–V, current–voltage; LCOE, levelized costs of electricity/energy; LED, light-emitting diode; m , meter; mc-Si, multicrystalline silicon; MI, moisture ingress; MID, moisture induced degradation; N, nitrogen; N, north; O, oxygen; Pb, lead; PID, potential induced degradation; P_{max} , maximum power; PV, photovoltaics; PVPS, Photovoltaic Power Systems Program; R_{ext} , external resistance; RH, relative humidity; R_{int} , internal resistance; SEM, scanning electron microscopy; Sn, tin; STC, Standard Test Conditions; T, temperature; TC, thermal cycling; Ti, titanium; T_m , module temperature; TPT, Tedlar[®]/Polyester/Tedlar[®]; UV, ultraviolet; UV-F, ultraviolet fluorescence spectroscopy; $V_{(x)}$, local voltage at a point x ; VI, visual inspection; V_{mpp} , voltage at maximum power point; V_{oc} , open circuit voltage; V_T , thermal voltage; β_{FF} , temperature coefficient of fill factor; β_{Jsc} , temperature coefficient of I_{sc} density; β_{Pmax} , temperature coefficient of P_{max} ; β_{Voc} , temperature coefficient of V_{oc} ; $\beta_{\eta m}$, temperature coefficient of efficiency; η_m , PV module efficiency; η_{Tref} , PV module efficiency at reference temperature; $\phi_{(x)}$, local luminescence at a point x ; ΔT , difference in cell temperature

^{*} Corresponding author.

E-mail address: oscar.k.segbefia@uia.no (O.K. Segbefia).

<https://doi.org/10.1016/j.egy.2023.01.126>

2352-4847/© 2023 The Author(s). Published by Elsevier Ltd. This is an open access article under the CC BY license (<http://creativecommons.org/licenses/by/4.0/>).

1. Introduction

The importance of solar energy in the Nordic countries is highlighted in Fig. 1 (IEA-PVPS, 2021). Usually, photovoltaic (PV) modules are expected to produce at least 90% and 80% of their rated power after 10 years and 25 years of operation, respectively (Köntges et al., 2014; Wohlgemuth et al., 2015). However, concerns of defects and fault modes associated with PV modules from environmental and climatic stressors such as temperature, humidity, ultraviolet radiation, wind and snow loads, soiling, etc. is worrying (Aghaei et al., 2022; Jordan and Kurtz, 2013; Wohlgemuth et al., 2015). These degradation and fault modes such as delamination, discolouration, metal grids corrosion, cracks, solar cell degradation, potential induced degradation (PID), interface adhesion losses, optical losses, and other material degradation affect modules' performance during their guarantee period of ca. 25 years or even more (Halwachs et al., 2019; Köntges et al., 2014; Liu et al., 2019; Wohlgemuth et al., 2015). These defects and fault modes lead to PV module degradation, and hence, power degradation (Jordan et al., 2012). About 2% of PV modules are predicted to fail after 11–12 years due to climatic stressors (Köntges et al., 2014). According to Jordan et al. (2012), PV plants

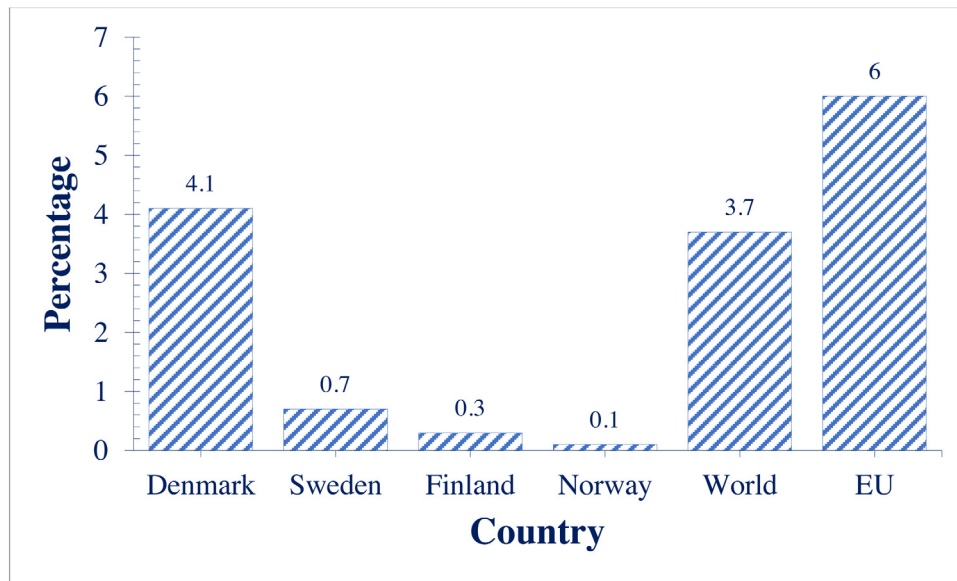


Fig. 1. Theoretical electricity contribution of PV to national energy mix, based on the PV capacity installed by the end of 2020 for the Nordics. Denmark is expected to exceed the world average electricity contribution from solar energy in the coming years.
Source: Extracted from IEA PVPS Snapshot of Global PV markets, 2021 (IEA-PVPS, 2021).

have an average degradation rate of 0.8%/year or more due to climatic defects.

PV module degradation can also be a function of the PV materials, usage, technology, assembling, and handling of PV modules (Aghaei et al., 2022; El Hammoumi et al., 2022; Halwachs et al., 2019; Jordan and Kurtz, 2013). From packaging to installation, estimated power loss of up to 1.43% (mainly due to cracks) was reported (Dhimish et al., 2022). Also, roof mounted PV modules are likely to operate at higher temperatures due to reduced ventilation, and for that matter tend to degrade faster (Jordan and Kurtz, 2013; Jordan et al., 2012). Crystalline silicon solar cells have annual degradation rates of ca. 0.5% while thin film technologies show annual degradation rate of 1% but are predicted to improve over the coming years (Jordan and Kurtz, 2013). In environments with high humidity and wind loads (such as in the Nordics), the reliability of PV modules is more complicated (Halwachs et al., 2019; Köntges et al., 2014; Papargyri et al., 2020).

Corrosion can cause parasitic resistance losses whilst delamination and discolouration of encapsulants can also lead to loss of adhesion and optical efficiency (Bosco et al., 2019; Halwachs et al., 2019; Köntges et al., 2017). Moisture ingress can induce most defect and failure modes which lead to PV module degradation and eventual power loss (Köntges et al., 2014). A comprehensive review on the effect of moisture ingress on the degradation of crystalline PV modules is provided by Segbefia et al. (2021b). Some defects and failure modes affect the appearance of the PV module, and are easily detected using visual inspection (Wohlgemuth et al., 2015). However, some others such as microcracks are difficult to detect with the unaided eye and have no effect on the appearance of the module but can affect the power output (Köntges et al., 2014; Tsanakas et al., 2016). For defects and fault modes that cannot be detected with visual inspection, advanced spectroscopic and microscopic techniques are used for their detection. Some of these tools are current–voltage (I–V) characterization, electroluminescence (EL), photoluminescence (PL), fourier transform infra-red (FTIR), ultraviolet fluorescence (UV-F) spectroscopy, thermography, scanning electron microscopy (SEM), and energy dispersive spectroscopy (EDS). However, these tools are only useful after a defect or fault mode has occurred and some are destructive.

Kurtz et al. (2017) defined qualification tests to be tests which naturally provide a pass or fail outcome which reflects whether the test artefact exceeds a minimum acceptable key indicator. These tests are carried on a representative sample of 10 or less modules and the tests are relatively short in duration and are done to minimize the cost of testing. Since 1970s, the qualification, testing and standardization for PV cells, modules, and systems have evolved tremendously (McMahon, 2004; Osterwald and McMahon, 2009). However, these tests are limited in identifying wear out failures and PV durability and reliability over their lifetime (Hacke et al., 2019; Tracy et al., 2018; Trout et al., 2017). Additionally, they are not reliable in detecting all defects and failure modes e.g. potential induced degradation (PID) (Hacke et al., 2018).

Accelerated ageing tests are promising in predicting wear out failures (Osterwald and McMahon, 2009). These ageing tests include thermal cycling (TC) tests, ultraviolet (UV) exposure, humidity freeze (HF) test, damp heat (DH), mechanical load tests or a combination of two or more in climatic or environmental chambers to identify specific defects and failure modes. One single approach does not test for all degradation modes, rather, other components of the PV module end up being aged undesirably during the testing of another factor (Bosco et al., 2019; Eder et al., 2018; Trout et al., 2017). The accumulation of acetic acid and lead acetate in the ethylene vinyl acetate (EVA) encapsulant after prolonged damp heat exposure which predisposes the cell to corrosion and subsequent degradation is an example (Bosco et al., 2019; Tracy et al., 2018). Hence, selecting the most effective ageing approach in order not to over-accelerate or under-accelerate these degradation factors is the key. Moreover, as modules' reliability and durability has improved in recent years, accelerated testing appears to be losing its effectiveness (Aghaei et al., 2022). The use of physical models to forecast PV module's durability and reliability is fast, convenient, and cost-effective. However, these models are amenable to errors in estimating climatic variables, degradation rates, and PV module reliability. This can introduce up to 65% variation in the estimated degradation rate values (Kaaya et al., 2021).

One keyway of reducing the levelized costs of electricity (LCOE) of PV systems is increasing the durability and reliability of these systems (Aghaei et al., 2022; Kazem et al., 2020; Soto et al.,

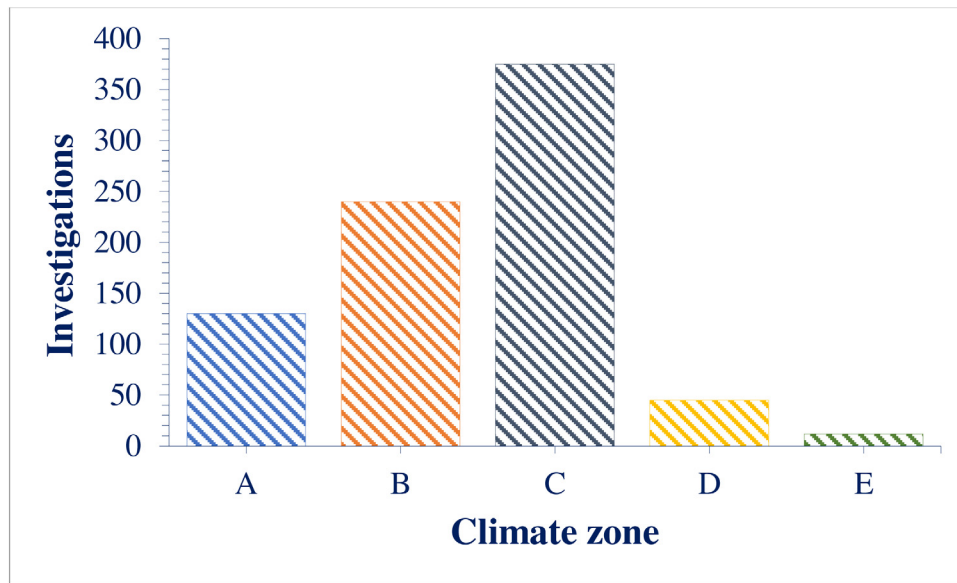


Fig. 2. Distribution of reported failure data on PV modules installed from the 1970s to the year 2015. Data is based on investigations that were done on the entire PV module as a unit.

Source: Extracted from Halwachs et al. (2019).

2022). According to a recent report by the researchers within the research project INFINITY in collaboration with the IEA PVPS Task 13 consortium and other multinational partners, there is an urgent need for collecting credible data on PV module performance and reliability globally (Halwachs et al., 2019). The report was collated based on the Köppen-Geiger climate zones: A (tropical), B (steppe/arid), C (temperate/moderate), D (cold/snow), and E (alpine/polar). The data for the study was collected on PV systems that were installed in the 1970s through to the year 2015. They found that most investigations were done in climate zones B and C except for investigations on PV module inverters. An extract of failure modes on investigations reported on the entire PV module as a unit is represented in Fig. 2. The Nordics fall in climate zone D, where the second fewest investigations were done over the study period, as expected.

Ample climatic failure data from each climate zone provides the platform for reliable correlation of expected failure mechanisms to specific climatic conditions and can provide useful insight into future investigations. Hence, practical field data from the cold regions (e.g., southern Norway) becomes ever more important. This work presents the main defects and failure modes associated with crystalline silicon PV modules deployed in Norway. To the best of our knowledge, we have not come across any such report from the same region. The work further investigates the underlying causes of the identified failure mechanisms using microstructural techniques. This distinguishes this study from the existing reports.

In the present work, the defects and fault modes of field-aged multicrystalline silicon (mc-Si) PV modules in a cold region are investigated. A catalogue of defects and fault modes together with the electrical performance data and temperature sensitivities of these modules is presented. In addition, the degradation rates of the PV modules over the initial 10 years of outdoor operation and the later 10 years when they were kept indoors is also presented. In Sections 2 and 3, a brief information on the Energy Park installed in Grimstad and the methods used for the defects and faults detection and diagnosis are presented, respectively. Finally, the results and insights from the investigation which

demonstrated that cracks and moisture ingress are the main root causes for the observed degradation in the field-aged PV modules, is presented in Section 4.

2. Background of the Energy Park at Dømmesmoen

There have been research efforts within the University of Agder on outdoor monitoring of PV modules' performance and reliability over the years. One of these pioneer installations is the Grimstad Renewable Energy Park installed in Dømmesmoen, Grimstad. The Energy Park was officially commissioned in June 2000 and consists of 96 multicrystalline silicon (mc-Si) PV modules, amorphous silicon (a-Si) panels, and thermal collectors (Våland et al., 1997). According to the manufacturer, these solar PV modules were certified as per the existing IEC 1215 (presently, the IEC 61215) standards. Currently, 43 of the mc-Si modules are available for investigation. The main purpose of the Energy Park was to serve as a resource center for research and education in renewable energy. In 2011, the PV modules were decommissioned and kept securely for research purposes. At the time of decommissioning, the electrical performance data of these modules was investigated by Verma et al. (2012), and it was found that the PV modules were producing ~90% of their rated power. However, their investigation on the mc-Si panels was solely on the electrical performance parameters, hence, the importance of the present study on the underlying defects and fault modes. A section of the park (mc-Si PV modules) and the geographical location of the installation site are shown in Fig. 3.

The climate in Grimstad (58.3447°N, 8.5949°E, 50 m above sea level for the installation site) is warm cold with monthly average temperature, relative humidity (RH), and air pressure ranges of −6.71 °C to 21.05 °C, 30% to 99%, and 97 kPa to 104 kPa, respectively. According to Köppen-Geiger climate classification, Grimstad is a humid continental climate, Dfb (−10 °C to +30 °C, with less than 90%), due to the constant stable marine air masses and heavy snow loads in winter (Beck et al., 2018). The optimum angle global irradiation is not more than 213 kWh/m². Average 1782 sunshine hours in a year with average wind speed between 3.4–5.3 m/s.

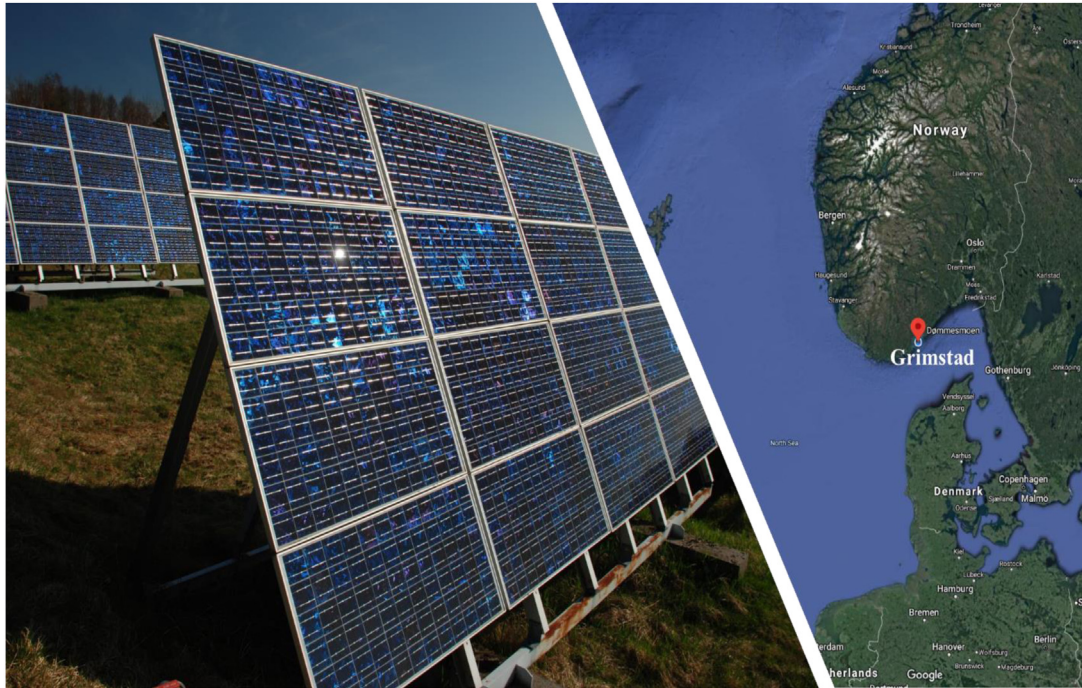


Fig. 3. A section of the mc-Si PV modules on the Energy Park at Dømmesmoen, Grimstad, showing the location of the site in southern Norway on the right.

3. Materials and methods

3.1. Materials

Defects and fault modes of the 43 field-aged mc-Si PV modules which have been installed in Grimstad between the years 2000 and 2011 are investigated using a combination of visual inspection (VI), current–voltage (I–V) characterization, ultraviolet fluorescence (UV-F), electroluminescence (EL), infrared (IR) thermal imaging, and scanning electron microscopy–energy dispersive spectroscopy (SEM-EDS) analysis. The schematic of the experimental method is illustrated in Fig. 4.

The technical specification of the solar cells and modules (as provided by the manufacturer in 2000) is summarized in Table 1. Details on the solar cell components and the module electrical layout was reported earlier (Segbefia et al., 2022; Segbefia and Sætre, 2022). By comparing the electrical performance characteristics to the information derived from the accompanying failure detection techniques, the underlying causes for power degradation of the PV modules were established. The characterization process took place partially indoors and outdoors.

3.2. Methods

3.2.1. Visual inspection

Visual inspection was conducted on all the PV panels (front and back) under clear sky outdoor and well-controlled light exposure conditions in the dark. This complementary procedure made it possible for a comprehensive logging of a variety of defects and fault modes which would not be possible with the conventional visual inspection alone. The visual inspection was done according to IEC 61215: 2016 standard.

3.2.2. I–V measurements

The current–voltage (I–V) characteristics (taken every two minutes) of all the PV panels was acquired using a handheld I–V 500w I–V Curve Tracer from HT[®] Instruments by following the

IEC 60904- 1 standard. The electrical parameters acquired via the I–V characterization are the maximum power (P_{max}), short circuit current (I_{sc}), maximum power point current (I_{mpp}), open circuit voltage (V_{oc}), maximum power point voltage (V_{mpp}) and fill factor (FF). The data included information on the in-plane irradiance (G_i), module temperature (T_m), and the normalized values of all the electrical parameters to Standard Test Conditions (STC) of each PV module. STC specifies cell temperature (T_c) of 25 °C, solar irradiance of 1000 W/m² and air mass 1.5 (AM1.5) spectrum for commercial PV panels. The I–V characterization of all the modules proceeded under clear sky outdoor G_i conditions (960–1060 W/m²), and the STC values were computed automatically by the I–V tracer used to minimize errors associated with data recording. The uncertainty of the Tracer for all the parameters (except the fill factor) measured is to the nearest hundredth. Moreover, the computed uncertainty is less than $\pm 3\%$ for all parameters measured. Hence, the values of all the parameters were approximated to the nearest tenth to accommodate the uncertainty in measurements. For the same reason, the FF and η_m are written in two significant figures. The PV module's efficiency (η_m) in the year 2020 was computed by multiplying the ratio of the normalized measured P_{max} values in the year 2020 to the datasheet P_{max} with the datasheet η_m value (13%). The relative temperature coefficients were determined using regression plots of electrical parameters (P_{max} , V_{oc} , I_{sc} , FF , η_m) versus T_m . The resulting regression equation fits the general linear equation: $y = mx + c$, where y and x denote the electrical parameter, x , and T_m , respectively. m and c represent the temperature coefficient (β_x) and intercept, respectively. The relative β_x in %/°C is then $\beta_x = m/c$. Details on the determination of β_x was presented earlier (Segbefia et al., 2021c; Segbefia and Sætre, 2022).

3.2.3. Ultraviolet fluorescence (UV-F) imaging

For the detection of moisture induced degradation (MID) defects and fault modes such as microcracks and optical degradation, the UV-F imaging technique is one of the handy tools. Moisture induced degraded PV module encapsulation materials

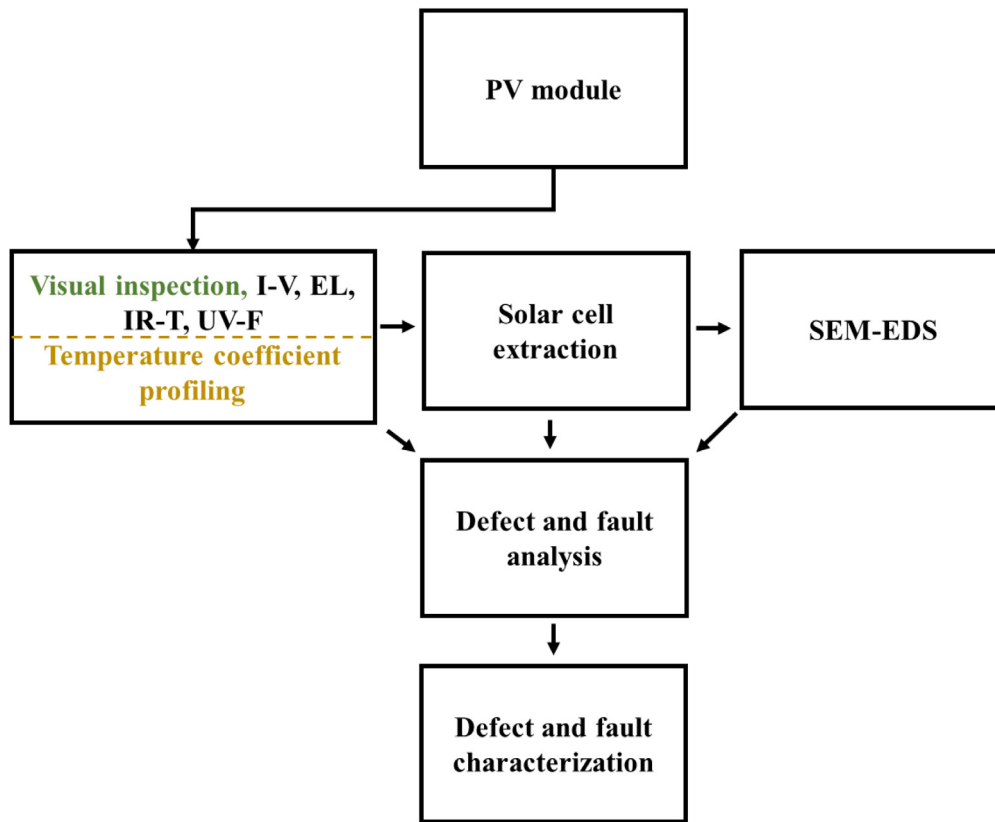


Fig. 4. Overview of the experimental methods.

Table 1
Solar module technical specification.

Module type	NESTE (NP100G12)
Power/efficiency (nameplate)	100 W ±10% (1000 W/m ² and 25 °C) η = 13 % (total area), FF = 70% V _{oc} = 21.6 V, I _{sc} = 6.7 A, I _{mpp} = 6.0 A, V _{mpp} = 16.7 V
Cells	Multicrystalline silicon
Module dimension	Area: 129.3 × 65 = 8'405 cm ² Depth: 3.4 cm (w. frame) Weight: 9.1 kg
Electrical layout	(12 × 2) × 3 = 72 cells in series
Front glass	Low iron content 3 mm tempered glass
Encapsulant	EVA (ethylene vinyl acetate)
Backsheet	Multi-layered TPT white (Tedlar [®] /Polyester/Tedlar [®])
Junction box	2 weatherproof plastic casing, accommodating a bypass diode each
Frame	Full perimeter anodized aluminum (Al-) frame

(e.g., EVA) show weak UV fluorescence due to photoquenching. When these encapsulation materials are exposed to UV light, degraded areas show darker traces. The acquired UV-F information becomes useful for defect cataloguing and mitigation. Each of the PV module was characterized using a portable TROTEC[®] LED UV TorchLight 15F (λ ≈ 365 nm) which is equipped with a Wolf eyes FD45 spectrum filter. The investigation was conducted in the dark by following the International Energy Agency (IEA) recommended procedure (Herrmann et al., 2021; Jahn et al., 2018).

3.2.4. Electroluminescence (EL) imaging

When a PV panel is forward biased, the solar cell signals in the infrared region can provide information on the degradation state of the PV panel. The EL characteristics of 15 sampled PV panels were acquired in a dark room using a BrightSpot EL Test Kit. The kit comprises of a 24 megapixels modified DSLR (digital single-lens reflex) Nikon D5600 camera, a DC power supply set,

connecting cables, a flexible tripod stand, and computer with data acquisition and processing software. The investigation was conducted by following the IEC 60904- 13 standard and the IEA procedure (Herrmann et al., 2021; Jahn et al., 2018). The EL characterization of the PV modules was conducted using forward bias current densities of 10% of I_{sc} and 100% of I_{sc}. In this investigation, 100% of I_{sc} is 6.7 A (datasheet value for I_{sc}) and 10% of I_{sc} is 0.67 A at ca. 23.76 V (110% of V_{oc}), refer to Table 1.

According to Potthoff et al. (2010), the local luminescence, φ_(x) at a point x of a PV module is related to the local voltage, V_(x) and the thermal voltage, V_T as

$$\phi_{(x)} = C_{(x)} \exp\left(\frac{V_{(x)}}{V_T}\right), \quad \text{for } V_{(x)} \gg V_T \quad (1)$$

Where C_(x) is the optical and material properties of the PV module and the camera system known as the local calibration factor. However, the operating voltage, V depends on V_(x), the internal

resistance (R_{int}) between the metal grids and the solar cells and external resistance (R_{ext}) between the interconnectors and the solar cells of the PV module and can be written as (Potthoff et al., 2010)

$$V = V_{(x)} + R_{int}I_{(x)} + R_{ext}I \quad (2)$$

Where $I_{(x)}$ is the local current flowing through point x of the solar cell and I is the total current supplied to the PV module. If the solar cell or module is in good condition, then $C_{(x)} \approx C$ for all solar cells in series (N_c) and R_{int} is negligible and $R_{ext} \approx R$, the total resistance within the PV module. Then V becomes (Potthoff et al., 2010)

$$V = V_T \cdot \ln\left(\frac{\phi_{(x)}}{C}\right) + I \cdot \frac{R}{N_c} \quad (3)$$

For a good solar cell and module, R is negligible at current density below 10% of I_{sc} (Potthoff et al., 2010). That is, higher voltages come with higher resistances from electrical contacts rather than bulk material resistances, when the module is in a good condition. But, at lower injection levels, the material properties dominate the luminescence signal of the PV module. However, for bad solar cells at current density below 10% of I_{sc} , $R \approx R_{int}$, and Eq. (3) could be written in the form of Eq. (1) for each solar cell as

$$\phi_{(x)} = C_{(x)} \exp\left(\frac{V_{(x)} + IR_{int}}{V_T}\right), \quad \text{for } V_{(x)} \gg V_T \quad (4)$$

In this case, the local luminescence is also influenced by the internal resistances as a result of cell cracks and other cell defects. In other words, when the cell is completely separated due to defects such as cracks, $I \approx I_{(x)} \approx 0$, and $V \approx V_{(x)}$ is maximum for the affected solar cell. However, moisture ingress can influence the luminescence signal due to photoquenching by degradation products, which is possible at open cracks or at the edges of the PV module.

That is, measurement at lower current density (ca. 10% of I_{sc}) is most appropriate for investigating degradation in material properties and measurements at higher current density (ca. 100% of I_{sc}) can be useful for evaluating the quality of the metal contacts. (Belmont et al., 2014; Jahn et al., 2018; Potthoff et al., 2010).

3.2.5. Infrared (IR) imaging

Defective PV panels under forward bias conditions can experience increased T_m due to the resistive losses. IR thermal information of the solar cells, and hence, the PV panel is useful for defects diagnostics. The IR thermal images of 15 sampled PV panels were acquired using the Fluke Ti400 Infrared Camera (measuring in the long-wave IR band: 650–1400 nm) by following the IEC 62446-3 standard. The investigation took place both indoors and outdoors. For the indoor investigation, the PV panels were investigated under I_{sc} forward bias conditions. IR images were taken 0.5, 2, and 5 min after current flow was initiated. For the outdoor investigation, the IR thermal images were acquired after soaking the PV panels in the sun for at least 15 min. For all measurements, the emissivity of the front glass and the TPT backsheets was set at 0.9 and 0.85, respectively. Details of the IR thermal imaging was presented earlier (Segbefia and Sætre, 2022).

3.2.6. Microstructural imaging of extracted solar cells

The defective areas were identified and extracted using a Water Jet NC 3060D Beveljet cutting machine. The Water Jet cutter uses a fine water jet stream with abrasive under ultra-high pressure (ca. 4,000 bar) for cutting a sample. This technique was preferred as low cutting temperatures was desired. The components of the as-cut cell sized samples were separated by treating

it with toluene. The samples were immersed in the solvent in custom-made container at room temperature for 14 days. The microstructural information on the extracted solar cell samples was acquired using SEM-EDS analyses. The analysis was done using a field emission scanning electron microscope (SEM) (JEOL 7200F) equipped with an energy dispersive X-ray spectrometer (Octane Elect EDS system from EDAX[®]-AMETEK[®]). Prior to the microstructural analysis, the extracted solar cell samples were rinsed carefully and thoroughly in isopropyl alcohol, then in deionized water, and finally air dried.

4. Results and discussion

4.1. Optical degradation

Defects and fault modes that affect the optical properties of a PV module include delamination, discolouration of encapsulants and degradation of the front glass (Tsanakas et al., 2016). For the purpose of this work, we will restrict optical degradation to delamination and discolouration of encapsulants as none of the modules has broken front glass. All modules were dirty as they have been kept indoors for ten years. As expected, per the visual inspection, signs of moisture ingress into these modules dominate along with indications of delamination at cell edges, discolouration of encapsulants, metal grids oxidation, trapped chemical species, and adhesion loss (especially at the edges of the modules) as shown in Figs. 5 and 6.

Fig. 5a is a part of one of the field-aged modules showing delamination at the cell edges and discolouration of encapsulant. Figs. 5b and 5c are extracted cells from the panel in Fig. 5a. Figs. 5d and 5e show the edges of some of the modules with loose Al-frame and signs of moisture ingress, grids corrosion, discolouration, and delamination of encapsulants, respectively. Moisture ingress from the modules' edges appears to be one of the dominant fault mechanisms (Segbefia et al., 2020). This is responsible for the optical degradation and other defects in the affected modules (Segbefia et al., 2021b). Corrosion of the metal parts of the bypass diodes of some of the modules in the junction box (Fig. 5f) lends more credence to the influence of moisture ingress. This is not surprising considering the climatic conditions of the Nordics, especially in Grimstad with a global annual average climate moisture index (CMI) greater than 0.6 (Willmott and Feddema, 1992), together with high wind and snow loads. Fig. 6 highlights some of the defects and faults modes observed in photographs acquired on the PV modules in a dark room. This step makes it possible to detect and diagnose defects and fault modes which were not visible with the traditional outdoor visual inspection alone.

This visual inspection step highlights degradation of front glass (Fig. 6a), oxidation of metal grids, especially at the points where the busbars are attached to the cells (Fig. 6b), discolouration of encapsulants (Fig. 6c), and trapped degradation species (Fig. 6d). The oxidation and corrosion of metal grids, solar cell, solder bonds, and loss of optical transparency (due to delamination and discolouration of front encapsulants) characterized almost all modules. The I–V curves of the module depicted in Fig. 7a at different module operating temperatures is illustrated in Fig. 7c. This is compared with the data sheet values quoted for the module at 25 °C. After 20 years, Fig. 7a show ~10% drop in the I_{sc} and ~4% drop in the V_{oc} for measurements at ca. 25 °C. However, when module temperature increases, the I_{sc} increases but marginally and the V_{oc} decreases significantly. That is, there is permanent degradation in I_{sc} .

The drop in both I_{sc} and V_{oc} indicates that these modules are suffering from both series and shunt resistances. One reason for the observed degradation mechanism is optical degradation.

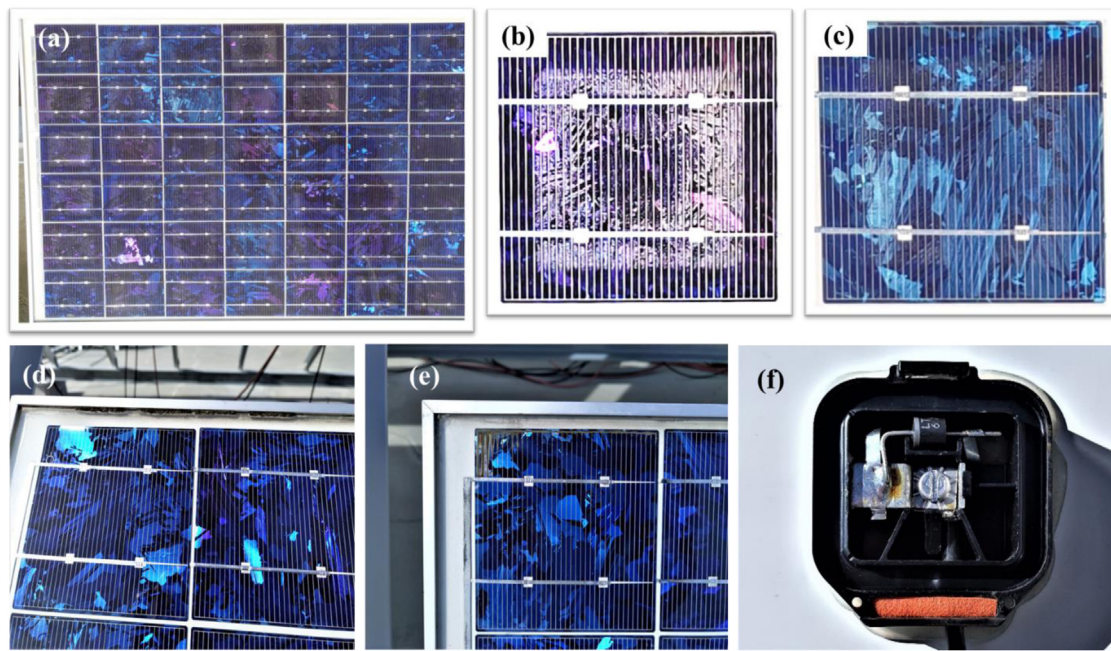


Fig. 5. Defects and fault modes from visual inspection. (a) A section of a field-aged PV module showing (b) delamination at cell edges, and (c) discoloration of encapsulant. Edges of modules with (d) loose Al-frames, and (e) signs of moisture ingress, grids corrosion, discoloration, and delamination of encapsulants. (f) A junction box showing signs of corrosion of the bypass diode and other metal interconnects. These images were acquired under clear sky outdoor conditions.

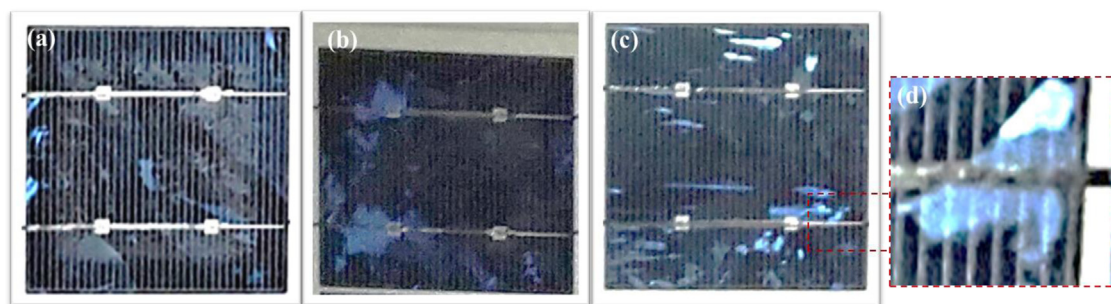


Fig. 6. Photographic images of cells from modules (taken in a dark room) showing signs of (a) corrosion of front glass, (b) oxidation of metal grids, (c) discoloration of encapsulants, and (d) metal grids corrosion and trapped degradation product in a zoomed-in image of the portion marked red in (c). (For interpretation of the references to colour in this figure legend, the reader is referred to the web version of this article.)

The main underlying cause of optical degradation is moisture ingress and UV radiation. However, optical degradation can also be a precursor for other fault mechanisms e.g., moisture ingress, microcracks, and corrosion which underline a degradation in V_{oc} . Of a greater concern is that optical degradation underlines short circuit (I_{sc}) degradation and can lead up to >50% drop in module efficiency (Al Mahdi et al., 2021). In addition, optical degradation can influence charge carrier absorption and transport properties within the PV module (Pern, 1993). This can lead to higher module temperature (degradation in temperature coefficients), and hence, a drop in efficiency (Dupré et al., 2015; Segbefia et al., 2021a).

4.2. Microcracks and cell degradation

Power loss due to cell cracks depends on several factors including the crack properties such as the crack size, geometry, location, orientation, and gravity. Cracks that damage the busbars and metal grids can result in power loss. A microcrack is a crack that has width less than 30 μm . However, the risk of power loss due to further degradation of microcracks into power sensitive cracks and defects under field operation is likely (Köntges et al.,

2014; Papargyri et al., 2020). Moreover, cell cracks can induce other defects such as snail trails, moisture ingress, delamination, corrosion, PID, etc. (Ohdaira et al., 2023). Fig. 8 shows the EL images of some of the field-aged modules with their corresponding UV-F images of the red marked out areas. The zoomed-in portions of the areas marked red in the EL and the UV-F images are placed at the top of each corresponding image. In Fig. 8a–c, EL images acquired under 100% of I_{sc} , are shown. Images acquired under this current density highlight metal contact problems such as broken and corroded contacts in darker marks, refer to Eq. (4). However, under 10% of I_{sc} , materials problems which are in darker shades are highlighted, see Fig. 8d–f. The darker appearances are as a result of the inability of current to reach these parts of the module under forward bias conditions due to defects. These defects are metal grids corrosion, degraded solar cells and solder bonds. In Fig. 8a–c, these degradations are highlighted as darker spots over the PV modules, especially along the busbars. In Fig. 8d–f, more defective cells are highlighted, some which were not visible in the EL images in Fig. 8a–c.

The presence of randomly distributed darker spots (Fig. 8a–c) and darker cells (Fig. 8d–f) over the modules suggests cells and material degradation.

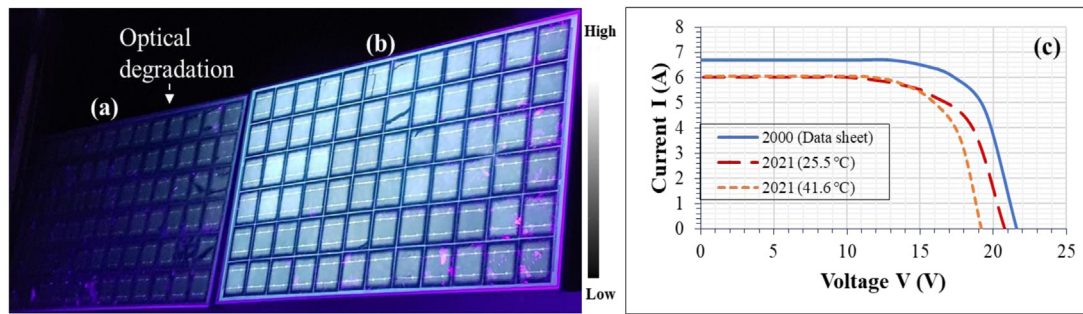


Fig. 7. UV-F images of (a) optically degraded and (b) fairly 'good' field-aged PV modules. (c) I–V characteristics of Fig. 7a at different module temperatures.

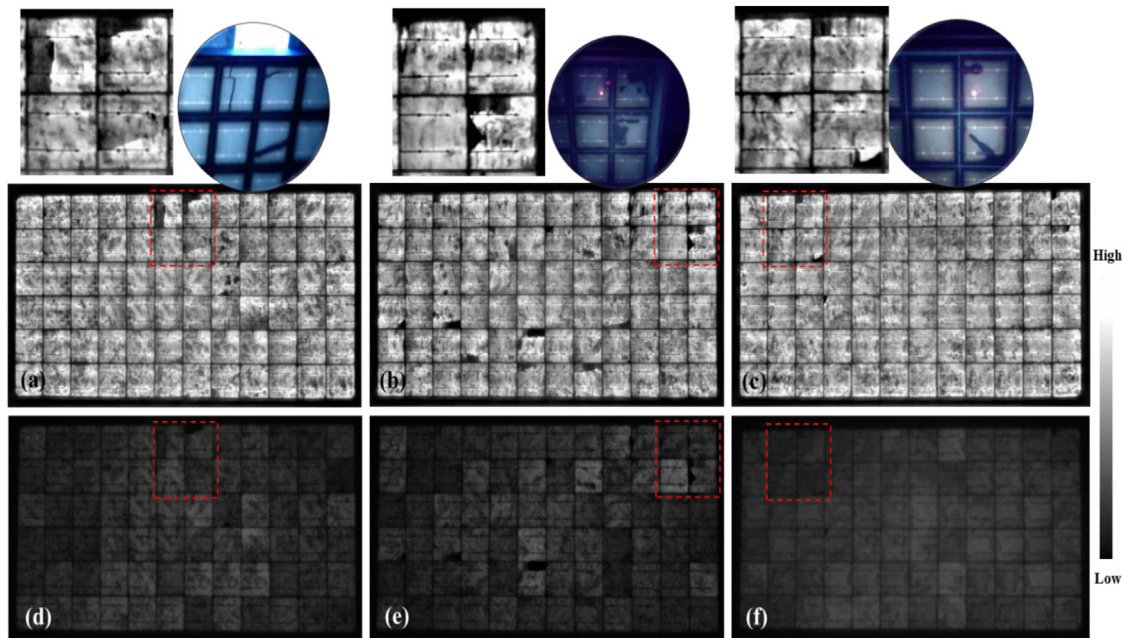


Fig. 8. EL images of 3 of PV panels under: (a)–(c) 100% of I_{sc} and (c)–(d) 10% of I_{sc} forward bias conditions. Areas marked in red are shown in corresponding zoomed-in EL images and UV-F images above.

One observation from Fig. 8d–f is that the majority of the less dark cells (better cells) are located in the middle parts of the PV module. Conversely, the majority of the darker cells (bad cells) are located at/near the edges of the module. Cells located at/near the perimeter of the modules are often more likely to be affected by moisture ingress. In addition, darker cells that are not located at the edge of the module appear to have underlining defect problem e.g., microcracks. This current accumulation at defective areas due to localized resistance leads to hotspots which can lead to accelerated ageing of the PV module. The observed defect patterns in the marked-out defective areas in the EL images are supported by the defect patterns in the UV-F images. The UV-F image of the marked-out portion of Fig. 8a shows critical microcracks. Moisture induced cell degradation is shown in the UV-F image of the marked-out portion of Fig. 8b. This cell degradation appears as a crack in the EL image, however. The UV-F image of the portion marked in Fig. 8c shows microcracks which have undergone further degradation due to moisture ingress.

Fig. 9 shows the IR thermal images of some of the field-aged modules. Fig. 9a–c are the IR thermal images acquired under real field outdoor conditions from the backside of the modules. The emissivity of the TPT backsheets was set at 0.85 for the outdoor measurements. Corresponding IR images acquired indoors under forward bias I_{sc} conditions after 5 min are shown in Fig. 9c–f. The indoor measurements were acquired from the front side of the

modules with emissivity of the front glass set at 0.9. The areas marked in the images show the defective areas highlighted in the EL images (refer to Fig. 8). The IR thermal images of the module in Fig. 8a are shown in Figs. 9a and 9d and the IR thermal images of the module in Fig. 8b are shown in Figs. 9c and 9f.

Hotspots from broken metal grids, cell cracks, and other defects are depicted with blue–red colour codes: areas with severe shunts and material defects correspond with darker red colour (Tsanakas et al., 2016). In Fig. 9, the IR images show comparable defects (cracks) location on the PV module as shown in the EL images in Fig. 8. However, the thermal patterns for outdoor and indoor tests vary. In Fig. 9a–c, the exact position of the defects is indicated with associated hotspots. However, in Fig. 9d–f, the positions of defective cells are not very clear. Under outdoor conditions, the hotspots characteristics depend on the photon absorption, charge carrier generation, recombination, and transport properties. These mechanisms are highly material dependent. On the other hand, indoor IR thermal imaging is much more reliant on charge carrier recombination and transport characteristics. Hence, defects and fault mechanisms are better highlighted in outdoor IR imaging. It was also observed that IR images acquired under indoor conditions in relatively shorter time periods (~ 1 min) could help to map out microcracks and other cell defects in PV modules. This could be done by comparing IR images taken at different time frames after the initiation of current

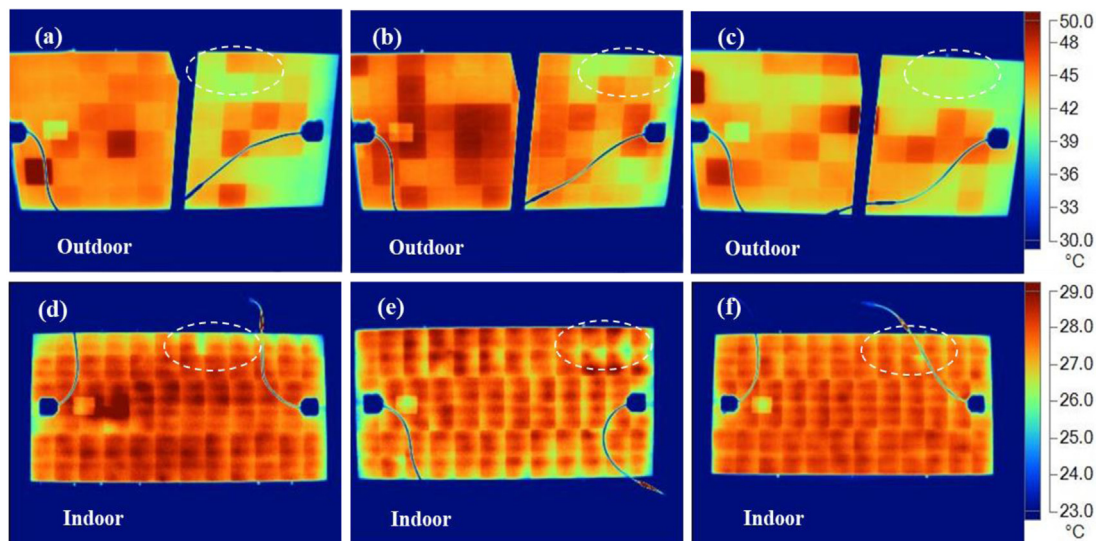


Fig. 9. IR thermal images acquired under (a)–(c) clear sky outdoor and (d)–(f) indoor forward bias I_{sc} conditions. Outdoor images were acquired after the modules were soaked in the sun for at least 15 min and the indoor images were taken 5 min after the forward bias current was initiated. The white marked areas show corresponding defective areas. The emissivity of the front glass (indoor measurements) and the TPT backsheets (outdoor measurements) was set at 0.9 and 0.85, respectively. The supporting frame (behind the PV module) in (a)–(c) and the cables show corresponding blue traces in the IR thermal images. (For interpretation of the references to colour in this figure legend, the reader is referred to the web version of this article.)

Table 2
Difference in cell temperature (ΔT) of different defect mechanisms that affected the PV modules under outdoor conditions.

Defect	ΔT (°C)	
	Result	Values from literature
Cracks	14 ± 2	2.5–45 (Buerhop et al., 2012; Tsanakas et al., 2016)
PID	7–15	7.5–30 (Jahn et al., 2018; Tsanakas et al., 2016)
Optical degradation	10 ± 2	6.0 ± 2 (Buerhop et al., 2012; Tsanakas et al., 2016)

flow. The temperature difference (ΔT) between the cell with the highest and lowest temperature in a PV module can be an indication of different defects and fault modes. It has to be noted, however, that ΔT values are also influenced by several factors including current characteristics and the ambient environment. In this regard, the ΔT values for the field-aged PV modules in each defect category was investigated. The average ΔT over the PV modules due to hotspots during the outdoor measurements was found for each defect category, see Table 2.

These values agree with observations elsewhere (Buerhop et al., 2012; Jahn et al., 2018; Tsanakas et al., 2016). According to Tsanakas et al. (2016), $\Delta T \approx 6 \pm 2$ °C indicates optical degradation such as delamination, trapped moisture bubbles, and discolouration of encapsulants. Critical solar cell cracks have been found to influence the thermal signatures of cells with ΔT values as high as ~ 45 °C (Buerhop et al., 2012; Tsanakas et al., 2016). However, for these modules, the spots with microcracks show $\Delta T \approx 14 \pm 2$ °C. Yet, the modules with microcracks show the highest ΔT . The ΔT values of the surrounding cells indicates that these cracks may be critical to current flow in the affected regions. Defective bypass diodes can also be a reason for the observed hotspots in Fig. 9. However, an inspection on the bypass diodes revealed that the bypass diodes are in good condition. Hence, the hotspots are a result of microcracks, and moisture induced defects e.g., corrosion, optical degradation, PID, etc.

4.3. Potential induced degradation (PID)

Typically, PID of the shunting type (PID-s) cells are identified as warmer cells in IR thermal images and darker cells in EL images, see Fig. 10. In Fig. 10, the EL and IR thermal images of one

of the PV modules affected by potential induced degradation (PID) are represented. EL images acquired under 100% of I_{sc} (Fig. 10a) and 10% of I_{sc} (Fig. 10b) are represented. In Fig. 10a, the luminescence intensity over the entire module is strong, though there are some localized darker spots, especially along the metal grids.

It is known that the electrical circuit is not always affected by corrosion and high series resistance. Hence, the effect of metal grids oxidation and the likes could be hidden in EL images if the grids are not significantly separated. Fig. 10b highlights PID and material defects localized to the edges of the module. The fact that a majority of the cells located nearer to the edges of the module are darker suggests that the degradation is due to moisture ingress from the perimeter of the module. This observation agrees with other reports on the influence of high humidity on the onset of PID (Ohdaira et al., 2023). In addition, the IR thermal image of this same module in Fig. 10c shows a fairly uniform distribution of temperature over its surface. It is therefore difficult to map out the defective cells or areas in Fig. 10c. In Fig. 10c, ΔT is ca. 3 °C. On the other hand, in Figs. 10b and 10d, the defective cells in the PV module correspond well and can be identified more easily. In Fig. 10d, ΔT is ca. 20 °C. The reason for the difference in the ΔT is due to the fact that the temperature sensitivity of defects is more highlighted under solar irradiation conditions than under induced current biasing conditions.

Also, the IR thermal images in Fig. 10d show cooler temperature regions around the cells, especially for cells at the edges of the module. Cooler temperature regions around cells in IR thermal images indicate PID-s degraded cells. It was also observed in the tests that, just at the initiation of current, cells and especially defective cells at the positive terminal show lower thermal profiles.

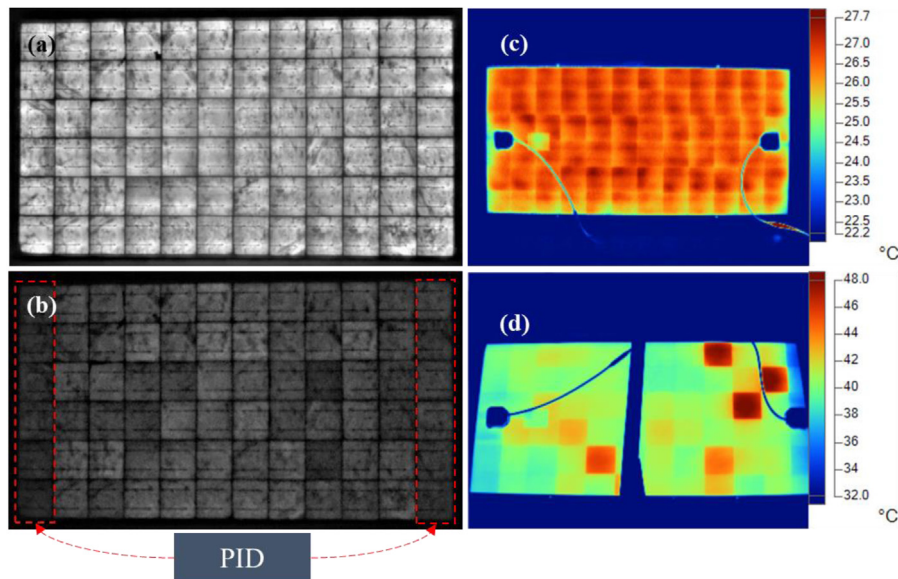


Fig. 10. A field-aged PV module affected by PID. EL images acquired under (a) 100% of I_{sc} and (b) 10% of I_{sc} . IR thermal image of the same module acquired under (c) indoor forward bias I_{sc} after 5 min and (d) clear sky outdoor conditions. In (c), $\Delta T \approx 3$ °C, and in (d), $\Delta T \approx 20$ °C. The supporting frame (behind the PV module) and the cables show corresponding blue traces in the IR thermal images.

4.4. Microstructural characteristics of the extracted solar cells

The EL signal in Fig. 10b could also be influenced by the interaction of moisture or moisture induced degradation (MID) chemical species. It is known that, water molecules absorb strongly in the near-infrared region (>0.70 microns) at ~ 20 °C (Curcio and Petty, 1951). However, the absorption of water in the UV region is negligible but is influenced by the amount of dissolved oxygen and/or other chemicals (Mason et al., 2016). Hence, the darker cells in Fig. 10b could also be due to absorption of the IR signals by suspected ingressed moisture or/and trapped MID species. Usually, cracks and delaminated regions in the module serve as reservoirs for moisture and moisture induced degradation products e.g., acetic acids (Segbefia et al., 2021b).

Fig. 11 shows the micro-structural characteristics of the solar cell extracted from the edge of the PV panel. The images were acquired from different regions of the same solar cell. Fig. 11a, 11b, and 11c show the SEM images with their corresponding EDS analyses shown in Fig. 11d, 11e, and 11f, respectively. Fig. 11a shows the degradation state of the solar cell extracted from the edge of the module. Fig. 11d shows the EDS point analysis of the 2 points in Fig. 11a. Point 1 has more oxygen (O) than Point 2. The presence of carbon (C) in Point 2 (Fig. 11d) suggests the presence of carboxylic acids (e.g., acetic acid) on the surface of the solar cells. The presence of these acids might have consequences for further degradation processes. The presence of carbon might be due to the degradation of EVA encapsulation and/or through the ingress of carbon dioxide into the module. The presence of C could also be due to traces of EVA left on the cell after the reclamation. Corrosion (due to MID) was observed to make the EVA encapsulation adhere more strongly to the solar cell at the points of corrosion. Also, moisture ingress is responsible for the traces of aluminum (Al) and tin (Sn) observed at Points 1 and 2 (Fig. 11d), as observed elsewhere (Kumar et al., 2019). The titanium comes from the TiO_2 antireflection coating (ARC) used for the solar cells (Segbefia et al., 2022).

Fig. 11b displays the SEM image of the solder of the cell with corresponding EDS analysis given in Fig. 11e. Solder material consists of Pb and Sn as indicated by the arrows in Fig. 11b. However, EDS analysis evidenced the oxidation of Pb which appears as large bright flakes in the image. Migration of tin on the surface of the

cell due to moisture (water and oxygen) ingress was also reported elsewhere (Kumar et al., 2019). The presence of oxygen at Point 1 in Fig. 11e confirms the observed oxidation around the metal grids as per the visual inspection (Fig. 6). Fig. 11c shows the state of the silver (Ag) grid of solar cells extracted from the edge of the field-aged PV modules. The Ag from the paste was oxidized as indicated by the presence of oxygen in the EDS analysis (Fig. 11f). This suggests that moisture ingress is the cause of the observed degradation modes. Similar degradation patterns were observed on polycrystalline silicon solar cells subjected to ca. 2500 h damp heat (DH) tests (Peike et al., 2013).

The degradation state of Ag and Pb and the presence of trace amounts of Sn, Al, C, and oxygen on the surface of the solar cells lend credence to the moisture induced degradation of these solar cells, see Fig. 11. Degradation of Ag and other elements in the Ag paste in the presence of moisture was also observed in other studies (De Rooij, 1989; Kumar et al., 2019; Moore and Codella, 1988; Nakano et al., 2016; Peike et al., 2013; Zheludkevich et al., 2004). According to Zheludkevich et al. (2004) and De Rooij (1989), the oxidation of Ag induces microcracks and flakes which facilitates the diffusion of oxygen, resulting in further degradation. Silver (I) oxide, AgO and silver (II) oxide, Ag_2O are the main MID products of silver in the case of PV application in the field (Kumar et al., 2019).

The presence of oxides of silver, lead, and other metals from the silver paste or solder on the surface of the cells lead to higher series resistance. In addition, the corrosion of the metal grids, solar cells, and the front glass due to the production of moisture induced degradation products is a precursor for shunts. Increased series resistance, reduced shunt resistance and degradation of the ARC lead to power degradation in the field-aged PV modules.

4.5. Power degradation

The distributions of the electrical characteristics (especially the P_{max}) can provide insight into the degradation state of PV modules. The I–V characteristics of PV modules were acquired under in-plane irradiance (960 – 1060 W/m^2) conditions, see Fig. 12. A clear spread in the P_{max} and I–V curves was observed. The difference in the electrical profiles' distribution is indicative of the degradation state of the modules after 20 years.

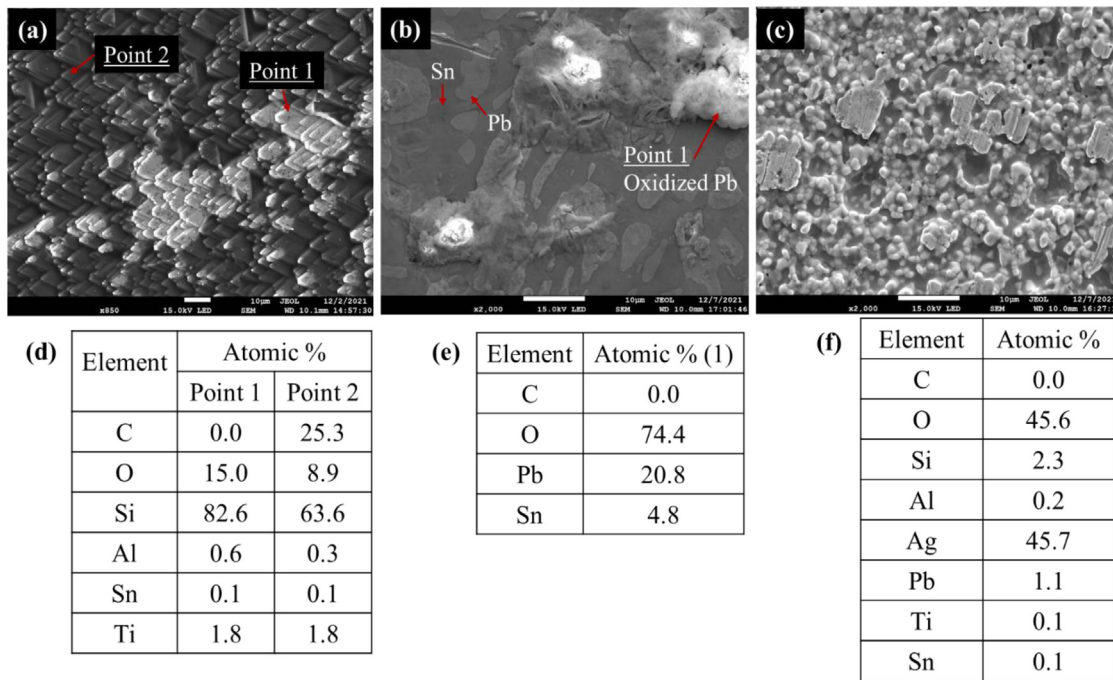


Fig. 11. SEM-EDS investigation of parts of solar cells extracted from the edge of the field-aged PV modules showing the effect of moisture ingress. Top row: (a) SEM image of solar cell showing degradation of the upper surface of the cell, (b) SEM image of the solder of the cell showing oxidation of lead (Pb), and (c) SEM image of the silver paste at the cell area where the grid is attached to the solar cell showing the state of the silver paste. Down row: Corresponding EDS analyses of (a), (b), and (c), respectively.

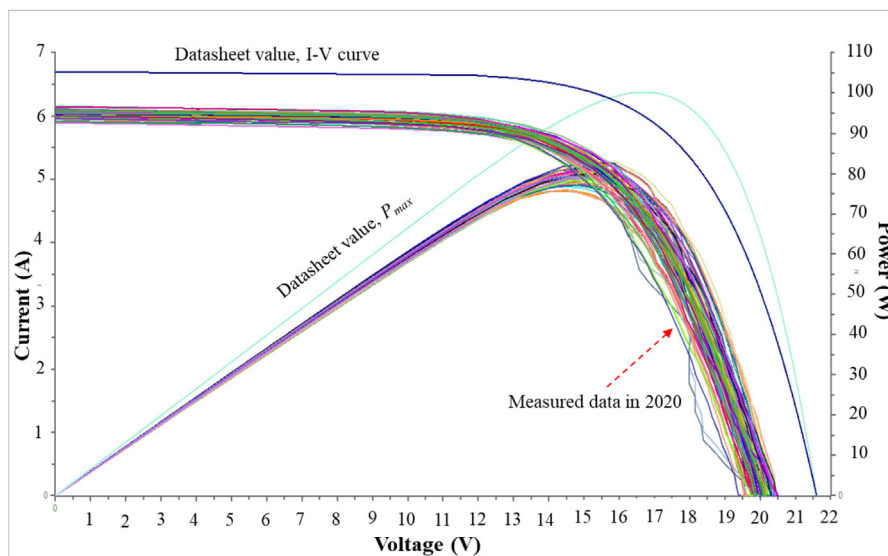


Fig. 12. Current–Voltage (I–V) and maximum power (P_{max}) curves of the PV modules under 960–1060 W/m^2 in-plane irradiance conditions normalized to STC.

The difference (Δ) in the electrical parameters of the PV modules was computed as the difference between the data sheet values and the values measured in the year 2020, according to a recommended procedure by Friesen et al. (2018) and Köntges et al. (2017). In Fig. 12, the difference in the I_{sc} (ΔI_{sc}) and V_{oc} (ΔV_{oc}) of the best and poorest PV modules are 4.9% and 4.31%, respectively. However, the change in P_{max} (ΔP_{max}) for the best and poorest modules was 14.8%. The value of ΔI_{sc} under the conditions in Fig. 12a is a strong indication of parasitic resistance losses which dominates at lower injection levels (Holman et al., 2012), as reported elsewhere (Dang et al., 2023). The average electrical parameters of the PV modules per technical data sheet from the manufacturer and measurements done in 2011 and 2020

are recorded in Table 3. The values for 2011 and 2020 are the average normalized values to STC.

In 2011, the modules were found to be producing $\sim 90\%$ of their nominal P_{max} (Verma et al., 2012). This value was within the tolerance limit (± 10) specified by the manufacturer as in Table 1. However, after 20 years (10 years in the field and another 10 years indoors), these modules are found to be producing $\sim 78\%$ of their nominal P_{max} . The degradation in the electrical parameters of these modules in 2020 normalized to STC is illustrated in Fig. 13. Fig. 13a shows the distribution of the electrical parameters (V_{oc} , I_{sc} , and FF as a function P_{max}) of these modules using a scatter plot. The randomness of these parameters, especially

Table 3
Average electrical parameters of the field-aged PV modules normalized to STC.

Year	P_{max} (W)	V_{oc} (V)	V_{mp} (V)	I_{mp} (A)	I_{sc} (A)	FF (%)	η (%)
2000	100	21.6	16.7	6.0	6.7	70	13
2011	90.2	21.5	16.1	5.1	6.2	68	12
2020	78.2	19.7	14.7	5.3	6.0	66	10

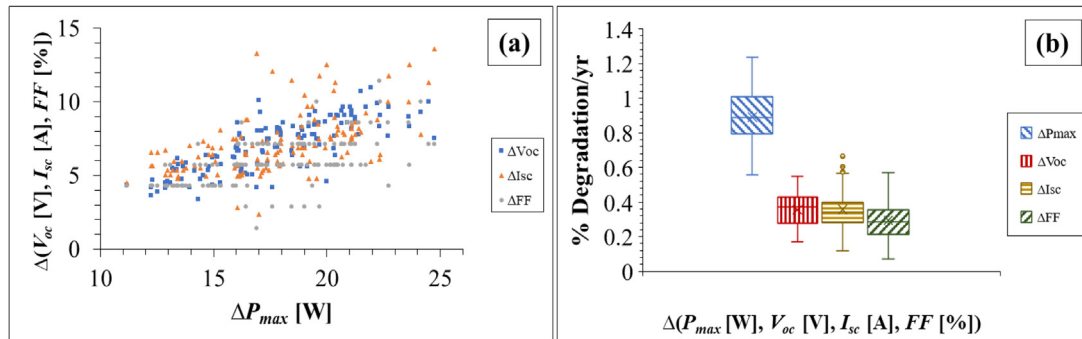


Fig. 13. Relative degradation in P_{max} , V_{oc} , I_{sc} and FF of the PV modules expressed as percentages. (a) A scatter plot showing the correlation among P_{max} , V_{oc} , I_{sc} , and FF degradation, (b) Box and whisker plots showing the five-number summary (that is the minimum, 25th percentile, median, 75th percentile, maximum, V_{oc} , I_{sc} , and FF of the PV modules. The edges of the boxes indicate the lower and upper quartiles. The internal lines and x-marks in the boxes indicate the median and mean, respectively. Δ is the difference between data sheet and measured values in 2020. The electrical performance data was acquired under 960 W/m²–1060 W/m² in-plane irradiance conditions, and then normalized to STC.

the I_{sc} , is uncharacteristic of ‘good’ PV cells or modules. Fig. 13b illustrates the degradation in the electrical parameters per year.

In Fig. 13b, the P_{max} degradation of all modules per year over the 20 years is above 0.5%; and more than 75% and 25% of the modules show annual degradation rates of >0.7% and >1.0% in P_{max} , respectively. Also, more than 75% of the modules showed an annual degradation rate of >0.2% in V_{oc} and I_{sc} , and more than 50% of them showed an annual degradation rate of more than 0.3% in V_{oc} and I_{sc} . However, only about 25% of the modules show an annual degradation rate of 0.3% or more in fill factor. Among all the electrical parameters, the V_{oc} and I_{sc} show mean degradation values just below and above their median values, respectively. This indicates that the V_{oc} and I_{sc} are skewed to the left (negatively skewed) and right (positively skewed), respectively. The difference in the mean and median values indicates degradation and this is the underlying cause of the overall P_{max} degradation, as observed elsewhere (Ohdaira et al., 2023; Virtuani et al., 2019). This also supports the observation in Fig. 14 which indicated a degradation in V_{oc} and I_{sc} as the underlying factors for P_{max} degradation.

It is known that P_{max} is linearly related to the V_{oc} , I_{sc} , and fill factor (FF) by:

$$P_{max} = V_{oc} \cdot I_{sc} \cdot FF \quad (5)$$

That is, any difference in the mean and median values of V_{oc} and I_{sc} affects the P_{max} of the PV modules. This is because V_{oc} and I_{sc} degradation also influence the FF degradation, and hence, leads to shunt losses (Annigoni et al., 2019; Halwachs et al., 2019; Köntges et al., 2014; Virtuani et al., 2019).

Fig. 14 highlights the degradation states of all the PV modules studied. A histogram of degradation rates per year showing the distribution of modules per their P_{max} degradation is shown in Fig. 14a. More than half (median or 50th percentile, P50) of the modules showed a degradation rate greater than 1.03 per year and not more than 10% (90th percentile, P90) of the modules showed a degradation below 1.17% per year. Over the entire 20 years, the annual degradation rate was computed to be 1.09%, a value which is greater than the 0.80%/year observed elsewhere (Jordan et al., 2012). Also, the average yearly degradation in the P_{max} of these PV modules over the first and second 10 years

periods are $\sim 0.98\%$ and $\sim 1.3\%$, respectively. These values are similar to the values reported for a similar climate by Belhaouas et al. (2022).

An average P_{max} of ~ 78 watts with a standard deviation of ca. 1.49 was recorded for the PV modules in 2020. Meanwhile, in 2011, the average power output and standard deviation were found to be ~ 90 watts and 0.41, respectively. This is also supported by the I–V curves of all the modules in 2011 and 2020, see Fig. 14b. Fig. 14b shows that the major factor for the degradation in P_{max} in 2011 is the degradation in the I_{sc} . This is due to high series resistance as reported elsewhere (Annigoni et al., 2019; Köntges et al., 2014). However, after these modules were kept indoors for a similar duration, degradation in V_{oc} dominates the underlying causes for P_{max} degradation. V_{oc} degradation is an indication of parasitic shunt losses which could be correlated to grave material degradation: metal grids corrosion, cracks, solder bond degradation, PID, etc. (Annigoni et al., 2019; Liu et al., 2019). According to Ohdaira et al. (2023), high humidity can induce PID-p. However, recovery of PID affected PV modules under sunshine is possible. These degradation mechanisms are due to moisture ingress, which is characteristic of the Nordics.

4.6. Degradation under indoor conditions

PV modules are expected to undergo minimal degradation (due to encapsulant discolouration) when kept indoors, where they are not exposed to any environmental stressor (Liu et al., 2019). It is known that optical degradation manifests itself in I_{sc} degradation (Annigoni et al., 2019; Köntges et al., 2014; Oh et al., 2019; Sinha et al., 2016). Yet, the I_{sc} degradation was minimal, and the degradation rates of the PV panels were higher when they were kept indoors. This degradation is mainly due to V_{oc} degradation, see Fig. 14b. It suggests that the higher degradation rate of the PV modules under indoor conditions after field exposure is mainly due to metal contact and material degradation issues. This also suggests FF degradation, refer to Fig. 13b. Degradation of the PV module components is due to the accumulation of volatile degradation products and subsequent formation of carboxylic acids (e.g., acetic acid) and other moisture induced degradation products during the later years.

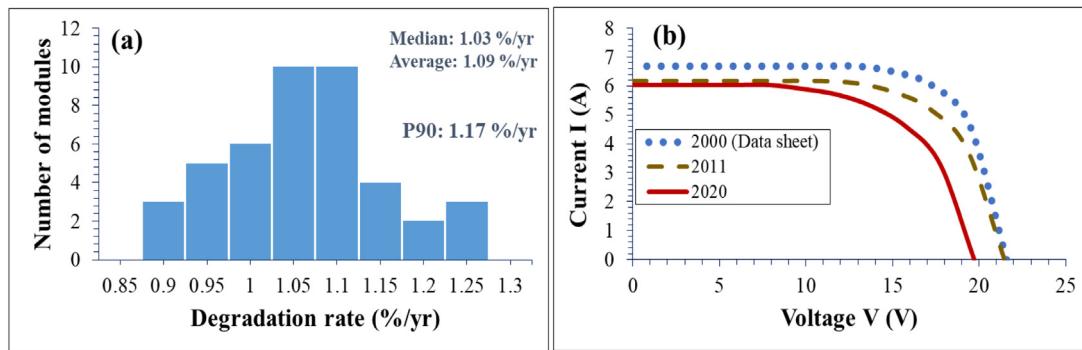


Fig. 14. (a) Degradation rates of all field-aged PV modules in 2020 showing the median, average, and 90th percentile (P90) values. (b) I–V curves of PV modules in 2000, 2011, and 2020.

Moisture (e.g., H₂O, O₂, CO₂, CO) ingress is the underlying cause of EVA degradation into acetic acid. The initial step in polymer (e.g., EVA) degradation is the formation of acetic acid, followed by polymer chain degradation (Allen et al., 2000; Oreski et al., 2017) and successive degradation of other PV module components. Yet, the formation of carboxylic acids such as acetic acids starts with the formation of carboxylic photoproducts (e.g., CO, CO₂, etc.) and moisture accumulation within the polymer substrate (Grossetête et al., 2000; Göpferich, 1996). Moreover, photodegradation products such as CO and CO₂ (which leads to the formation of acetic acids and its coproducts) are photo- and thermally unstable and oxidizes and evaporate at temperatures up to ca. 100 °C (Grossetête et al., 2000).

These modules were exposed to environmental stressors including high humidity conditions. Hence, the likelihood of the formation of photoproducts within the PV module during the field exposure is high. In the field, these volatile degradation products have the possibility to escape when the module heats up during operation. Conversely, under indoor conditions, evaporation of these volatile products is limited, and formation and accumulation of MID products is more feasible. The retention of these carboxylic radicals and ingressed moisture (during field exposure) within the module can result in the formation of carboxylic acids e.g., acetic acid (Oreski et al., 2017). This can induce defects and fault modes such as solar cell degradation, corrosion, delamination, and discoloration of encapsulants leading to considerable degradation in V_{oc} as observed elsewhere (Ohdaira et al., 2023). This is believed to be responsible for the significant power loss and higher degradation rate observed in 2020.

4.7. Temperature sensitivity of the PV modules

The effect of PV module's operating temperature on output power is well known (Dupré et al., 2015; Green, 2003; Skoplaki and Palyvos, 2009). Moreover, PV cell parameters such as V_{oc} , I_{sc} , and FF tend to vary linearly when temperature varies (Dupré et al., 2015). So, from Eq. (5), the overall temperature coefficient of P_{max} ($\beta_{P_{max}}$) could be expressed in terms of the temperature coefficients of open circuit voltage ($\beta_{V_{oc}}$), short circuit current density ($\beta_{J_{sc}}$), and fill factor (β_{FF}). This can be written as

$$\beta_{P_{max}} = \beta_{V_{oc}} + \beta_{J_{sc}} + \beta_{FF} \quad (6)$$

However, each of these parameters in Eq. (6) depends on different loss mechanisms in the PV module (Green, 2003). In addition, Eq. (5) tells us that the fill factor influences the amount of power that could be extracted from a PV module with current-voltage tradeoffs. These tradeoffs mainly depend on the generation and recombination balances and the resistance losses at P_{max} (Dupré et al., 2015). Yet, the generation and recombination

losses depend on material quality, which could be measured using the V_{oc} . That is, the V_{oc} of a PV cell is the measure of the carrier generation–recombination balance. So, the temperature sensitivity of a PV cell or module improves with increasing V_{oc} . In addition, it is known that the $\beta_{V_{oc}}$ of a solar cell accounts up to ~90% of the overall temperature sensitivity of the solar cell (Dupré et al., 2015). Hence, degradation in the $\beta_{V_{oc}}$ affects P_{max} the most, and indicates some form of material degradation.

A graph of temperature sensitivities as a function of in-plane irradiance (G_i) and PV module operating temperature (T_m) of the PV modules are represented in Fig. 15. The dependence of the temperature coefficients on G_i is shown in Fig. 15a. The inconsistent spread in the $\beta_{P_{max}}$ and β_{FF} indicates that the modules are at various stages of degradation.

This is clearly evident in the Box and whisker plots in Fig. 15b, where the relative changes in the temperature coefficients are quantified. From Fig. 15b, the $\beta_{P_{max}}$ degradation depends strongly on the β_{FF} , $\beta_{V_{oc}}$, and $\beta_{J_{sc}}$ degradation. That is, the observed degradation in the $\beta_{P_{max}}$ is as a result of the β_{FF} degradation. β_{FF} depends mainly on $\beta_{V_{oc}}$ and $\beta_{J_{sc}}$ characteristics which are products of parasitic resistance losses. Usually, temperature coefficients are normalized, refer to Eq. (6). Hence, any mechanism that influences the efficiency of the solar cell alters its temperature sensitivity, and vice versa. Fig. 15b suggests that the $\beta_{P_{max}}$ for the modules varies from 0.1–0.8%/°C. From Fig. 15b, over 75% of the PV modules show less than 0.1%/°C change in $\beta_{J_{sc}}$ while the same fraction of the modules shows more than 0.1%/°C change in FF . Conversely, all the modules show a relative change in $\beta_{V_{oc}}$ which is greater than 0.1%/°C. It is obvious then that the major underlying factor for the degradation in both $\beta_{P_{max}}$ and β_{FF} is the $\beta_{V_{oc}}$ degradation, which usually comes from shunt losses due to the junction quality of solar cells.

The influence of temperature on the efficiency of the PV modules is illustrated in Fig. 16. A graph of the Evans–Florschuetz efficiency ratio (η_m/η_{Tref}) versus T_m is shown in Fig. 16a. According to Evans and Florschuetz (1978), this ratio can be used to determine the nominal or the data sheet temperature coefficient of efficiency (β_{η_m}) value of crystalline silicon modules when the data sheet value for β_{η_m} is not available. For these PV modules, information on the temperature coefficients was not provided in the data sheet by the manufacturer. So, the Evans–Florschuetz efficiency ratio versus temperature plot was used to estimate the β_{η_m} of the modules. The normalized module efficiency versus T_m in the year 2020 is shown in Fig. 16b. Fig. 16a reflects the ideal temperature sensitivity of the modules when they were in a relatively good condition, and the temperature sensitivity of these modules in their current condition is reflected in Fig. 16b. This suggests that the nominal (data sheet) temperature coefficient of efficiency of the PV modules was ca. $-0.4\%/^{\circ}\text{C}$ (Fig. 16a) and has degraded to ca. $-0.5\%/^{\circ}\text{C}$ (Fig. 16b) over the 20 years period.

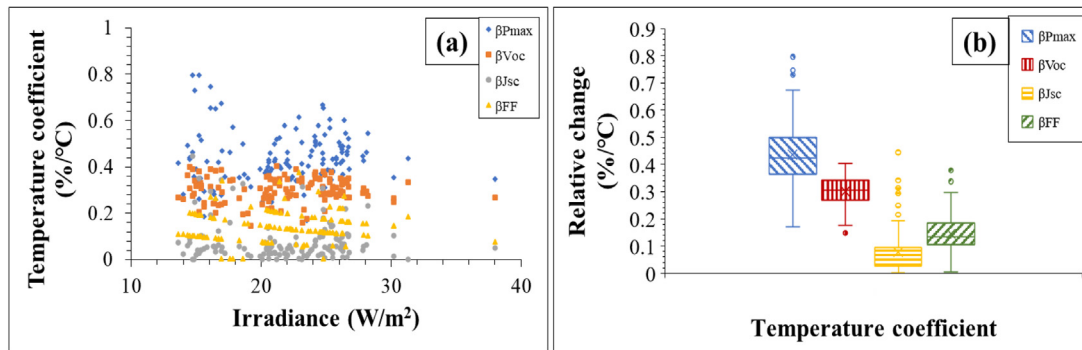


Fig. 15. Variation of (a) temperature coefficients with in-plane solar irradiance. (b) Variation in the temperature coefficients of electrical parameters of the PV modules. The edges of the boxes indicate the lower and upper quartiles and the internal lines and x-marks in the box indicate the median and mean, respectively. The electrical performance data was acquired under 960 W/m²–1060 W/m² in-plane irradiance conditions, and then normalized to STC.

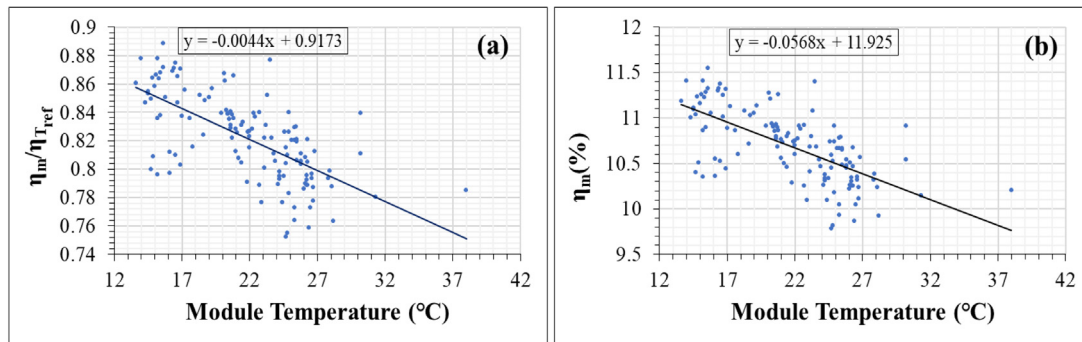


Fig. 16. The influence of temperature sensitivity on the efficiency of the PV modules. A graph of (a) Evans–Floschuetz efficiency ratio (η_m/η_{Tref}) and (b) normalized η_m versus T_m . The electrical performance data was acquired under 960 W/m²–1060 W/m² in-plane irradiance conditions, and then normalized to STC.

Degradation in the temperature coefficients of the PV modules leads to linear degradation in P_{max} . Hence, the observed degradation in the temperature coefficients suggests that the modules have undergone significant degradation. Also, Fig. 16b suggests that when T_m is ~ 25 °C and by extrapolation, the average efficiency of the modules reduces to $\sim 10\%$, which agrees with the value reported in Table 1 for the year 2020. However, when the T_m is 0 °C and by extrapolation, η_m is ca. 12% (refer to Fig. 16b). The η_m of the PV modules is not expected to be lower than the data sheet value (13%) if the PV modules are in good condition. This also supports the earlier evidence from the visual inspection, I–V characteristics, EL images, IR thermal images, and SEM-EDS analysis which points strongly to material degradation in the PV modules due to moisture ingress.

Taken together, these results suggest that the PV modules have been affected by a variety of defects and fault modes as a result of moisture ingress. In addition, the presence of microcrack can lead to moisture ingress, and vice versa. Hence, both have been observed as co-defects. Field-aged solar PV modules suffer from multiple defect mechanisms. In this work, efforts have been made to select modules with dominant defects for the investigation of specific defect mechanisms. Yet, the influence of other inherent defects on the overall investigation cannot be ruled out. At least three modules were used to investigate each defect category. In addition, over 20 years, PV technologies have revolved tremendously. More investigations in the cold regions utilizing newer and larger number of state-of-the-art technologies will be needed to improve and reemphasize the findings in this work.

Conclusion

PV plants are susceptible to varying degradation modes due to climatic and environmental stressors. As such, PV performance

reliability studies is very important to develop credible climate specific protocols to ensure that PV plants produce optimal power consistently over their guaranteed lifetime. This will minimize the payback time on investment and levelized cost of electricity of PV plants and boost the confidence level in PV energy sources. Investigations on the 20 years old PV modules suggest that the major defects and fault modes affecting these modules is moisture ingress and microcracks (co-defects), which are precursors for other degradations modes. I–V characterization, UV-F, IR thermal, and EL imaging were used for defects and fault modes diagnosis. SEM-EDS analysis confirmed that the PV modules are affected by moisture ingress. The modules were found to be affected by MID defects such as microcracks, optical degradation, corrosion, PID, and the degradation of the solar cells and solder bonds.

It was observed that more than 93% of the modules were affected by optical degradation, and the average P_{max} of the modules decreased to $\sim 78\%$, a 22% degradation which is more than the 20% degradation limit specified for good PV modules. In addition, the temperature coefficient of efficiency of the modules has also degraded to $-0.5\%/^{\circ}\text{C}$ after 20 years. FF and V_{oc} degradation appear to dominate the root cause of P_{max} degradation. However, the I–V characteristics suggest that the modules have been affected by both serial and shunt resistance losses. Also, it has been found that the average annual degradation rate of the modules was $\sim 1.09\%$. Yet, the degradation rates of the modules in the first 10 years (when they were in the field) and the later 10 years (when they were kept indoors) were $\sim 0.98\%/year$ and $\sim 1.33\%/year$, respectively. Consequently, the average efficiency of the modules dropped from 13% to $\sim 10\%$. In summary, moisture ingress underlines the observed degradation in the electrical parameters in the PV modules.

CRedit authorship contribution statement

Oscar Kwame Segbefia: Conceptualization, Methodology, Investigation, Validation, Writing – original draft. **Naureen Akhtar:** Investigation, Validation, Writing – review & editing. **Tor Os-kar Sætre:** Conceptualization, Supervision, Writing – review & editing, Funding acquisition.

Declaration of competing interest

The authors declare that they have no known competing financial interests or personal relationships that could have appeared to influence the work reported in this paper.

Data availability

Data will be made available on request.

Acknowledgement

The authors acknowledge the continuous support of the University of Agder, Norway.

References

- Aghaei, M., Fairbrother, A., Gok, A., Ahmad, S., Kazim, S., Lobato, K., Oreski, G., Reinders, A., Schmitz, J., Theelen, M., 2022. Review of degradation and failure phenomena in photovoltaic modules. *Renew. Sustain. Energy Rev.* 159, 112160.
- Al Mahdi, H.A., Leahy, P.G., Morrison, A.P., 2021. Predicting early EVA degradation in photovoltaic modules from short circuit current measurements. *IEEE J. Photovolt.*
- Allen, N.S., Edge, M., Rodriguez, M., Liauw, C.M., Fontan, E., 2000. Aspects of the thermal oxidation, yellowing and stabilisation of ethylene vinyl acetate copolymer. *Polym. Degrad. Stab.* 71 (1), 1–14.
- Annigoni, E., Virtuani, A., Caccivio, M., Friesen, G., Chianese, D., Ballif, C., 2019. 35 Years of photovoltaics: Analysis of the TISO-10-kW solar plant, lessons learnt in safety and performance—Part 2. *Progr. Photovolt. Res. Appl.* 27 (9), 760–778.
- Beck, H.E., Zimmermann, N.E., McVicar, T.R., Vergopolan, N., Berg, A., Wood, E.F., 2018. Present and future Köppen–Geiger climate classification maps at 1-km resolution. *Sci. Data* 5 (1), 1–12.
- Belhaouas, N., Mehareb, F., Kouadri-Boudjelthia, E., Assem, H., Bensalem, S., Hadjrioua, F., Aissaoui, A., Hafdaoui, H., Chahtou, A., Bakria, K., 2022. The performance of solar PV modules with two glass types after 11 years of outdoor exposure under the mediterranean climatic conditions. *Sustain. Energy Technol. Assess.* 49, 101771.
- Belmont, J., Olakonu, K., Kuitche, J., TamizhMani, G., 2014. Degradation rate evaluation of 26-year-old 200 kW power plant in a hot-dry desert climate. In: 2014 IEEE 40th Photovoltaic Specialist Conference. PVSC, IEEE, pp. 3162–3166.
- Bosco, N., Moffitt, S., Schelhas, L.T., 2019. Mechanisms of adhesion degradation at the photovoltaic module's cell metallization-encapsulant interface. *Prog. Photovolt., Res. Appl.* 27 (4), 340–345.
- Buerhop, C., Schlegel, D., Niess, M., Vodermayr, C., Weißmann, R., Brabec, C., 2012. Reliability of IR-imaging of PV-plants under operating conditions. *Sol. Energy Mater. Sol. Cells* 107, 154–164.
- Curcio, J.A., Petty, C.C., 1951. The near infrared absorption spectrum of liquid water. *JOSA* 41 (5), 302–304.
- Dang, D.N., Le Viet, T., Takano, H., Duc, T.N., 2023. Estimating parameters of photovoltaic modules based on current–voltage characteristics at operating conditions. *Energy Rep.* 9, 18–26.
- De Rooij, A., 1989. The oxidation of silver by atomic oxygen. *ESA J.* 13 (4), 363–382.
- Dhimish, M., Ahmad, A., Tyrrell, A.M., 2022. Inequalities in photovoltaics modules reliability: From packaging to PV installation site. *Renew. Energy* 192, 805–814.
- Dupré, O., Vaillon, R., Green, M.A., 2015. Physics of the temperature coefficients of solar cells. *Sol. Energy Mater. Sol. Cells* 140, 92–100.
- Eder, G.C., Voronko, Y., Dimitriadis, S., Knöbl, K., Újvári, G., Berger, K.A., Halwachs, M., Neumaier, L., Hirschl, C., 2018. Climate specific accelerated ageing tests and evaluation of ageing induced electrical, physical, and chemical changes. *Prog. Photovolt., Res. Appl.*
- El Hammoumi, A., Chtita, S., Motahhir, S., El Ghzizal, A., 2022. Solar PV energy: From material to use, and the most commonly used techniques to maximize the power output of PV systems: A focus on solar trackers and floating solar panels. *Energy Rep.* 8, 11992–12010.
- Evans, D., Florschuetz, L., 1978. Terrestrial concentrating photovoltaic power system studies. *Sol. Energy* 20 (1), 37–43.
- Friesen, G., Herrmann, W., Belluardo, G., Herteleer, B., 2018. Photovoltaic Module Energy Yield Measurements: Existing Approaches and Best Practice. Report IEA-PVPS T13-11 2018, pp. 25–26.
- Göpferich, A., 1996. Mechanisms of polymer degradation and erosion. *Biomaterials* 17 (2), 103–114.
- Green, M.A., 2003. General temperature dependence of solar cell performance and implications for device modelling. *Prog. Photovolt. Res. Appl.* 11 (5), 333–340.
- Grossetête, T., Rivaton, A., Gardette, J., Hoyle, C.E., Ziemer, M., Fagerburg, D., Clauberg, H., 2000. Photochemical degradation of poly (ethylene terephthalate)-modified copolymer. *Polymer* 41 (10), 3541–3554.
- Hacke, P.L., Kempe, M.D., Wohlgemuth, J., Li, J., Shen, Y.-C., 2018. Potential-Induced Degradation-Delamination Mode in Crystalline Silicon Modules. National Renewable Energy Lab.(NREL), Golden, CO (United States).
- Hacke, P., Owen-Bellini, M., Kempe, M., Miller, D.C., Tanahashi, T., Sakurai, K., Gambogi, W.J., Trout, J.T., Felder, T.C., Choudhury, K.R., 2019. Combined and sequential accelerated stress testing for derisking photovoltaic modules. In: *Advanced Micro-and Nanomaterials for Photovoltaics*. Elsevier, pp. 279–313.
- Halwachs, M., Neumaier, L., Vollert, N., Maul, L., Dimitriadis, S., Voronko, Y., Eder, G., Omazi, A., Mühleisen, W., Hirschl, C., 2019. Statistical evaluation of PV system performance and failure data among different climate zones. *Renew. Energy* 139, 1040–1060.
- Herrmann, W., Eder, G., Farnung, B., Friesen, G., Köntges, M., Kubicek, B., Kunz, O., Liu, H., Parlevliet, D., Tsanakas, I., 2021. Qualification of photovoltaic (pv) power plants using mobile test equipment. In: *IEA-PVPS T13-24: 2021*.
- Holman, Z.C., Descoeudres, A., Barraud, L., Fernandez, F.Z., Seif, J.P., De Wolf, S., Ballif, C., 2012. Current losses at the front of silicon heterojunction solar cells. *IEEE J. Photovolt.* 2 (1), 7–15.
- IEA-PVPS, 2021. International Energy Agency. 2021 Snapshot of global PV markets - task 1: strategic PV analysis and outreach.
- Jahn, U., Herz, M., Köntges, M., Parlevliet, D., Paggi, M., Tsanakas, I., 2018. Review on Infrared and Electroluminescence Imaging for PV Field Applications: International Energy Agency Photovoltaic Power Systems Programme: IEA PVPS Task 13. Subtask 3.3: report IEA-PVPS T13-12: 2018, International Energy Agency.
- Jordan, D.C., Kurtz, S.R., 2013. Photovoltaic degradation rates—an analytical review. *Prog. Photovolt., Res. Appl.* 21 (1), 12–29.
- Jordan, D.C., Wohlgemuth, J.H., Kurtz, S.R., 2012. Technology and Climate Trends in PV Module Degradation. National Renewable Energy Lab.(NREL), Golden, CO (United States).
- Kaaya, I., Ascencio-Vásquez, J., Weiss, K.-A., Topič, M., 2021. Assessment of uncertainties and variations in PV modules degradation rates and lifetime predictions using physical models. *Sol. Energy* 218, 354–367.
- Kazem, H.A., Chaichan, M.T., Al-Waeli, A.H., Sopian, K., 2020. Evaluation of aging and performance of grid-connected photovoltaic system Northern Oman: Seven years' experimental study. *Sol. Energy* 207, 1247–1258.
- Köntges, M., Kurtz, S., Packard, C., Jahn, U., Berger, K.A., Kato, K., Friesen, T., Liu, H., Van Iseghem, M., Wohlgemuth, J., 2014. Review of failures of photovoltaic modules.
- Köntges, M., Oreski, G., Jahn, U., Herz, M., Hacke, P., Weiß, K.-A., 2017. Assessment of Photovoltaic Module Failures in the Field: International Energy Agency Photovoltaic Power Systems Programme: IEA PVPS Task 13. Subtask 3: Report IEA-PVPS T13-09: 2017, International Energy Agency.
- Kumar, S., Meena, R., Gupta, R., 2019. Imaging and micro-structural characterization of moisture induced degradation in crystalline silicon photovoltaic modules. *Sol. Energy* 194, 903–912.
- Kurtz, S., Repins, I.L., Hacke, P.L., Jordan, D., Kempe, M.D., Whitfield, K., Phillips, N., Sample, T., Monokroussos, C., Hsi, E., 2017. Qualification Testing Versus Quantitative Reliability Testing of PV-Gaining Confidence in a Rapidly Changing Technology. National Renewable Energy Lab.(NREL), Golden, CO (United States).
- Liu, Z., Castillo, M.L., Youssef, A., Serdy, J.G., Watts, A., Schmid, C., Kurtz, S., Peters, I.M., Buonassisi, T., 2019. Quantitative analysis of degradation mechanisms in 30-year-old PV modules. *Sol. Energy Mater. Sol. Cells* 200, 110019.
- Mason, J.D., Cone, M.T., Fry, E.S., 2016. Ultraviolet (250–550 nm) absorption spectrum of pure water. *Appl. Opt.* 55 (25), 7163–7172.
- McMahon, T., 2004. Accelerated testing and failure of thin-film PV modules. *Prog. Photovolt., Res. Appl.* 12 (2–3), 235–248.
- Moore, W.M., Codella, P.J., 1988. Oxidation of silver films by atomic oxygen. *J. Phys. Chem.* 92 (15), 4421–4426.
- Nakano, M., Fujiwara, T., Koga, N., 2016. Thermal decomposition of silver acetate: physico-geometrical kinetic features and formation of silver nanoparticles. *J. Phys. Chem. C* 120 (16), 8841–8854.

- Oh, W., Bae, S., Kim, S., Park, N., Chan, S.-I., Choi, H., Hwang, H., Kim, D., 2019. Analysis of degradation in 25-year-old field-aged crystalline silicon solar cells. *Microelectron. Reliab.* 100, 113392.
- Ohdaira, K., Akitomi, M., Chiba, Y., Masuda, A., 2023. Potential-induced degradation of n-type front-emitter crystalline silicon photovoltaic modules—Comparison between indoor and outdoor test results. *Sol. Energy Mater. Sol. Cells* 249, 112038.
- Oreski, G., Mihaljevic, A., Voronko, Y., Eder, G.C., 2017. Acetic acid permeation through photovoltaic backsheets: Influence of the composition on the permeation rate. *Polym. Test.* 60, 374–380.
- Osterwald, C., McMahon, T., 2009. History of accelerated and qualification testing of terrestrial photovoltaic modules: A literature review. *Prog. Photovolt., Res. Appl.* 17 (1), 11–33.
- Papargyri, L., Theristis, M., Kubicek, B., Krametz, T., Mayr, C., Papanastasiou, P., Georgiou, G.E., 2020. Modelling and experimental investigations of microcracks in crystalline silicon photovoltaics: A review. *Renew. Energy* 145, 2387–2408.
- Peike, C., Hoffmann, S., Hülsmann, P., Thaidigsmann, B., Weiß, K., Koehl, M., Bentz, P., 2013. Origin of damp-heat induced cell degradation. *Sol. Energy Mater. Sol. Cells* 116, 49–54.
- Pern, F., 1993. Luminescence and absorption characterization of ethylene-vinyl acetate encapsulant for PV modules before and after weathering degradation. *Polym. Degrad. Stab.* 41 (2), 125–139.
- Potthoff, T., Bothe, K., Eitner, U., Hinken, D., Köntges, M., 2010. Detection of the voltage distribution in photovoltaic modules by electroluminescence imaging. *Prog. Photovolt. Res. Appl.* 18 (2), 100–106.
- Segbefia, O.K., Akhtar, N., Sætre, T.O., 2022. The effect of moisture ingress on titania antireflection coatings in field-aged photovoltaic modules. In: 2022 IEEE 49th Photovoltaics Specialists Conference, PVSC, IEEE, pp. 1237–1244.
- Segbefia, O.K., Imenes, A.G., Burud, I., Sætre, T.O., 2021a. Temperature profiles of field-aged multicrystalline silicon photovoltaic modules affected by microcracks. In: 2021 IEEE 48th Photovoltaic Specialists Conference, PVSC, IEEE, pp. 0001–0006.
- Segbefia, O.K., Imenes, A.G., Sætre, T.O., 2020. Outdoor fault diagnosis of field-aged multicrystalline silicon solar modules. In: 37th EU PVSEC.
- Segbefia, O.K., Imenes, A.G., Sætre, T.O., 2021b. Moisture ingress in photovoltaic modules: A review. *Sol. Energy* 224, 889–906.
- Segbefia, O.K., Paudyal, B.R., Burud, I., Sætre, T.O., 2021c. Temperature coefficients of photovoltaic modules under partial shading conditions. In: 38th EU PVSEC. pp. 1180–1186.
- Segbefia, O.K., Sætre, T.O., 2022. Investigation of the temperature sensitivity of 20-year old field-aged photovoltaic panels affected by potential induced degradation. *Energies* 15 (11), 3865.
- Sinha, A., Sastry, O., Gupta, R., 2016. Nondestructive characterization of encapsulant discoloration effects in crystalline-silicon PV modules. *Sol. Energy Mater. Sol. Cells* 155, 234–242.
- Skoplaki, E., Palyvos, J.A., 2009. On the temperature dependence of photovoltaic module electrical performance: A review of efficiency/power correlations. *Sol. Energy* 83 (5), 614–624.
- Soto, E.A., Arakawa, K., Bosman, L.B., 2022. Identification of target market transformation efforts for solar energy adoption. *Energy Rep.* 8, 3306–3322.
- Tracy, J., D’hooge, D.R., Bosco, N., Delgado, C., Dauskardt, R., 2018. Evaluating and predicting molecular mechanisms of adhesive degradation during field and accelerated aging of photovoltaic modules. *Prog. Photovolt., Res. Appl.* 26 (12), 981–993.
- Trout, T.J., Gambogi, W., Felder, T., Choudhury, K., Garreau-Iles, L., Heta, Y., Stika, K., 2017. PV Module Durability-connecting field results, accelerated testing, and materials. In: 2017 IEEE 44th Photovoltaic Specialist Conference, PVSC, IEEE, pp. 2312–2317.
- Tsanakas, J.A., Ha, L., Buerhop, C., 2016. Faults and infrared thermographic diagnosis in operating c-Si photovoltaic modules: A review of research and future challenges. *Renew. Sust. Energ. Rev.* 62, 695–709.
- Våland, T., Bartholdsen, W., Ottestad, M., Våge, M., 1997. Grimstad Renewable Energy Park. Agder University College, NO-4878 Grimstad, Norway. <http://ieahia.org/pdfs/grimstad.pdf>.
- Verma, D., Tayyib, M., Sætre, T.O., Midtgård, O.-M., 2012. Outdoor performance of 10 year old a-Si and poly-Si modules in southern Norway conditions. In: 2012 38th IEEE Photovoltaic Specialists Conference, IEEE, pp. 002368–002371.
- Virtuani, A., Caccivio, M., Annigoni, E., Friesen, G., Chianese, D., Ballif, C., Sample, T., 2019. 35 Years of photovoltaics: Analysis of the TISO-10-kW solar plant, lessons learnt in safety and performance—[part] 1. *Prog. Photovolt. Res. Appl.* 27 (4), 328–339.
- Willmott, C.J., Feddema, J.J., 1992. A more rational climatic moisture index. *Prof. Geogr.* 44 (1), 84–88.
- Wohlgemuth, J., Silverman, T., Miller, D.C., McNutt, P., Kempe, M., Deceglie, M., 2015. Evaluation of PV module field performance. In: 2015 IEEE 42nd Photovoltaic Specialist Conference, PVSC, IEEE, pp. 1–7.
- Zheludkevich, M., Gusakov, A., Voropaev, A., Vecher, A., Kozyrski, E., Raspopov, S., 2004. Oxidation of silver by atomic oxygen. *Oxid. Met.* 61 (1), 39–48.